Journal of Physical Organic Chemistry

WILEY

Journal of Physical Organic Chemistry

RESEARCH ARTICLE OPEN ACCESS

Triplet 4-Nitrenemethyl-Pyridine-*N*-Oxide: A Model Alkyl Nitrene Isolated in Cryogenic Matrices

Cláudio M. Nunes[1] | A. J. Lopes Jesus[2] | Tatiana Caneca[1] | Gemma Aragay[3] | Pablo Ballester[3,4] | Rui Fausto[1,5]

[1]University of Coimbra, CQC-IMS, Department of Chemistry, Coimbra, Portugal | [2]CQC-IMS, Faculty of Pharmacy, Coimbra, Portugal | [3]Institute of Chemical Research of Catalonia (ICIQ), the Barcelona Institute of Science and Technology (BIST), Tarragona, Spain | [4]ICREA, Barcelona, Spain | [5]Spectroscopy@IKU, Faculty Sciences and Letters, Department of Physics, Istanbul Kultur University, Istanbul, Turkey

Correspondence: Cláudio M. Nunes (cmnunes@qui.uc.pt)

Received: 13 January 2026 | **Revised:** 5 February 2026 | **Accepted:** 7 February 2026

Keywords: IR spectroscopy | matrix-isolation | nitrenes | photochemistry | quantum chemical calculations

ABSTRACT

Alkyl nitrenes are highly reactive intermediates that are particularly challenging to study experimentally. Here, we report the first investigation of the simplest triplet alkyl nitrene bearing a pyridine-*N*-oxide moiety. Direct irradiation ($\lambda > 350$ nm) of 4-azidomethyl-pyridine-*N*-oxide in an Ar matrix (15 K) generated the target triplet 4-nitrenemethyl-pyridine-*N*-oxide ^{3}**2**, along with *E* and *Z* isomers of 4-iminomethyl-pyridine-*N*-oxide **3**. Results from subsequent irradiations ($\lambda > 325$ nm) enabled the discrimination of the IR spectroscopic signatures of these species, allowing their unequivocal identification with support from DFT-B3LYP computations. Triplet nitrene ^{3}**2** was found to be stable in dark Ar matrices, demonstrating that quantum tunneling 1,2-H shift to imine **3** is not operative on the experimental timescale. Computations show that this reaction is thermodynamically favorable on the triplet surface but involves a high-energy barrier (~36 kcal mol^{-1}), explaining the absence of H-tunneling. As the pyridine-*N*-oxide moiety can act as an anchoring site for complexation with calix[4]pyrrole derivatives, our findings open new perspectives for investigating alkyl nitrene reactivity and tunneling phenomena under supramolecular confinement conditions.

1 | Introduction

Nitrenes are reactive intermediates characterized by a monovalent nitrogen center bearing six valence electrons, whose properties strongly depend on their molecular structure and spin multiplicity [1, 2]. Among the various classes of nitrenes, alkyl nitrenes remain particularly challenging to study experimentally. In contrast to their aryl counterparts, the lack of significant electronic delocalization at the nitrene center renders alkyl nitrenes extremely reactive and difficult to characterize.

Attempts to generate the simple methylnitrene [CH_3N] via thermal or photochemical denitrogenation of methyl azide [CH_3N_3] have eluded both time-resolved spectroscopic detection and trapping by bimolecular reagents [1]. Direct photolysis experiments of methyl azide in cryogenic matrices could only identify the corresponding methyleneimine [$CH_2{=}NH$][1,2] [3–7]. Methylnitrene was characterized as possessing a triplet ground state that lies ~31.2 kcal mol^{-1} lower in energy than the singlet state [8]. Computations at the CASPT2 level indicate that singlet methylnitrene is a true minimum on the potential energy surface (PES), although it is separated by a very low barrier of 2–3 kcal mol^{-1} from the 1,2-hydrogen shift to methyleneimine, with an exothermicity exceeding 80 kcal mol^{-1} [9]. Supporting this rationalization, a collision-free photochemistry study of methyl azide (248 nm), probed by tunable synchrotron radiation–based photoionization, indicated direct N_2 loss and singlet methylnitrene formation, which rapidly rearranges to yield the vibrationally excited methanimine preluding intersystem crossing (ISC) to the triplet state [10].

Journal of Physical Organic Chemistry, 2026; 39:e70074
https://doi.org/10.1002/poc.70074

Substitution of the labile α-hydrogen atoms in alkyl nitrenes by fluorine allowed Platz et al. to generate triplet trifluoromethylnitrene [CF_3N] by photolysis (254 nm) of trifluoromethylazide [CF_3N_3] in cryogenic matrices and to characterize it by EPR and UV-Vis spectroscopy [11]. According to CASSCF(8,8)/6-31G* computations, singlet trifluoromethylnitrene is separated by a barrier of 10 kcal mol^{-1} from a 1,2-fluorine shift to the corresponding imine [$CF_2{=}NF$], with an overall exothermicity of 46 kcal mol^{-1}. The authors postulated that the enhanced stability of singlet trifluoromethylnitrene toward unimolecular 1,2-migration, relative to singlet methylnitrene, renders ISC an effectively competing process, thereby enabling experimental observation of the corresponding triplet alkyl nitrene. In contrast, substitution with methyl groups did not sufficiently deactivate the rapid 1,2-migration, as the photolysis study of *tert*-butyl azide [$(CH_3)_3CN_3$] in cryogenic matrices could only identify the isomeric imine [$(CH_3)_2C{=}NCH_3$] [12]. Even the photolysis study of the bridgehead alkyl azides, 1-azidoadamantane and 1-azidonorbornane, in cryogenic matrices, showed efficient rearrangement to isomeric imines, and only trace amounts of the corresponding triplet nitrenes were detected by EPR spectroscopy [13, 14].

To circumvent the ultrafast singlet-state 1,2-migration in alkylnitrenes, direct access to the less reactive triplet alkyl nitrenes has been pursued via triplet-sensitized approaches [15]. Using this strategy, Gudmundsdottir et al. employed alkyl azides bearing an intramolecular ketone triplet sensitizer, such as in derivatives of 2-azido-1-phenylethanone [$PhCOCH_2N_3$] and 3-azido-1-phenylpropan-1-one [$PhCOCH_2CH_2N_3$] [16, 17]. Upon UV irradiation, these systems enabled reasonably efficient generation of triplet alkyl nitrenes allowing their characterization by laser flash photolysis in solution and by steady-state spectroscopic techniques in cryogenic matrices. Notably, these triplet alkyl nitrenes have been reported to behave as relatively persistent intermediates in solution, with lifetimes of microseconds, and rather than undergoing rapid hydrogen abstraction from the solvent, they predominantly dimerize to form azo products.

Although previous studies demonstrated access to triplet alkyl nitrenes, investigations into their generation and reactivity remain limited. Our interest in nitrene species has focused on developing model systems that enable investigations of fundamental aspects of quantum tunneling reactivity [18–23]. Aiming to access triplet nitrenes putatively capable of exhibiting intramolecular H-shift reactions while minimizing undesired bimolecular side reactions, we envisioned producing them from 1:1 complexes of 4-azido-(alkyl)-pyridine-*N*-oxide derivatives with tetra-α aryl-extended calix[4]pyrrole AE-C[4]P receptors (Scheme 1) [24–26]. The pyridine-*N*-oxide moiety functions as an anchoring group to produce thermodynamically ($K > 10^4\,M^{-1}$) and kinetically ($k_{off} < 0.1\,s^{-1}$) highly stable 1:1 complexes in both chlorinated organic solvents and water. One of the simplest nitrene derivatives that fits this strategy is triplet 4-nitrenemethyl-pyridine-*N*-oxide **^{3}2**, an alkyl nitrene bearing two α-hydrogen atoms capable of 1,2-H shift (Scheme 1). As a first step toward this broader goal, herein we report an initial study exploring the feasibility of generating **^{3}2** via direct photolysis of the selected 4-azidomethyl-pyridine-*N*-oxide **1** precursor under cryogenic matrix-isolation conditions. The results provide the inaugural characterization of this triplet alkyl nitrene species, including preliminary insights into its chemical nature.

2 | Experimental and Computational Section

2.1 | Synthesis

4-Azidomethyl-pyridine-*N*-oxide **1** was prepared by *N*-oxidation of 4-azidomethyl pyridine following a described procedure using Oxone as oxidant [27]. In turn, 4-azidomethyl pyridine was obtained uneventfully by reacting 4-bromomethylpyridine hydrobromide with sodium azide in DMF solution using potassium carbonate as base [28].

1: ^{1}H NMR (400 MHz, 298 K, $CDCl_3$): δ (ppm) = 8.19 (d, *J* = 6.8 Hz, 2H), 7.22 (d, *J* = 6.8 Hz, 2H), 4.39 (s, 2H).

^{13}C NMR (100 MHz, 298 K, $CDCl_3$): δ (ppm) = 139.4, 134.3, 125.1, 52.43.

HR-MS (APCI+) m/z: $[M+H]^+$ calculated for $C_6H_7N_4O^+ = 151.0614$, found 151.0613.

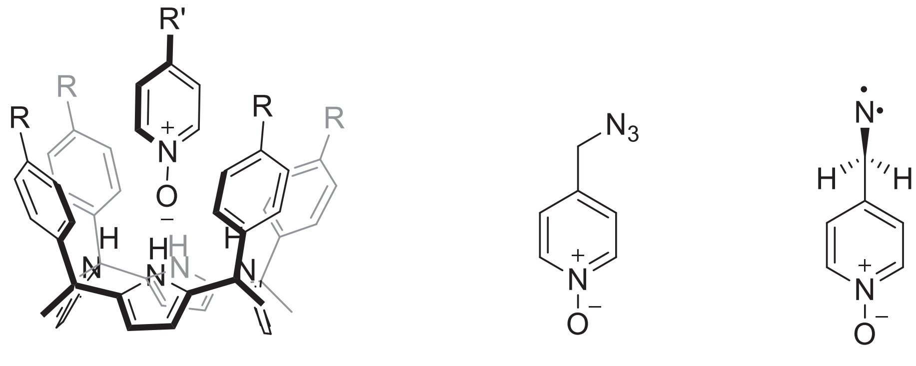

pyridine-*N*-oxide⊂AE-C[4]P **1** **^{3}2**

SCHEME 1 | (a) Line-drawing structure of the 1:1 complex of pyridine-*N*-oxide and a tetra-α isomer of an aryl-extended calix[4]pyrrole receptor illustrating our proposed strategy for nitrene stabilization. (b) Molecular structures of triplet 4-nitrenemethyl-pyridine-*N*-oxide **^{3}2**, for which we report the results on its generation in cryogenic matrices using 4-azidomethy-pyridine-*N*-oxide **1** precursor.

2.2 | Matrix-Isolation IR Spectroscopy

A sample of azide **1** was placed in a custom-built oven connected to the vacuum chamber of a closed-cycle helium cryostat (APD Cryogenics model HC-2, equipped with a DE-202A expander) and pumped to remove any volatile impurities. Prior to matrix deposition, the chamber pressure reached ~2×10^{-6} mbar. Vapors of **1** were generated by gently heating the sample to ~45°C using a thermoelectric power supply (Vitecom DC Power Supply, model 75-HY5003). The resulting vapors were co-deposited with a large excess of high-purity argon (N60, Air Liquide) onto a CsI optical window maintained at 15 K. The temperature was measured directly at the sample holder by using a silicon diode sensor connected to a digital controller (Scientific Instruments, model 9650-1), providing a temperature stabilization with an accuracy of ±0.1 K. Matrix preparation was monitored by recording IR spectra to optimize deposition and ensure conditions for isolating a monomeric sample. IR spectra were collected in the mid-infrared region (4000–400 cm^{-1}) at a resolution of 0.5 cm^{-1} using a Thermo Nicolet 6700 FTIR spectrometer equipped with a deuterated triglycine sulfate (DTGS) detector and a germanium/potassium bromide (Ge/KBr) beamsplitter. The instrument was continuously purged by a stream of dry air to minimize interference from moisture and CO_2.

2.3 | UV-Vis Irradiation Experiments

UV-Vis irradiation was conducted through the outer quartz window of the cryostat using a 250 W Hg (Xe) arc lamp (Newport, Oriel Instruments). The lamp output was passed through an 8 cm water filter and long-pass optical filters with cutoff wavelengths of 350 or 325 nm.

TABLE 1 | Optimized geometries of conformers **1g** and **1t**, relative zero-point-corrected energies (ΔH_{0K}, kJ mol^{-1}), relative Gibbs free energies at 298 K (ΔG_{298K}, kJ mol^{-1}), and the respective Boltzmann populations at the same temperature (*Pop.*, %), computed at the B3LYP/6-311+G(2d,p) and DPLNO-CCSD(T)/def2-TZVPP//ωB97XD/6-311+G(2d,p) levels, respectively[a].

	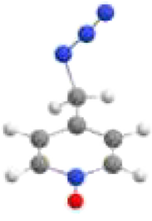 **1g**	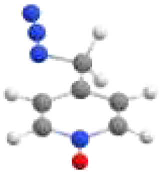 **1t**
ΔH_{0K}	0.00 | 0.00	0.41 | 1.94
ΔG_{298K}	0.00 | 0.00	0.29 | 0.55
Pop.	54 | 56	46 | 44

[a]Relative Gibbs free energies were corrected for conformational degeneracy by including the term $-RT\ln(g)$, where g is the number of equivalent minima associated with each conformer ($g=4$ for **1g** and $g=2$ for **1t**; see Figure S1). Color scheme: carbon (gray), nitrogen (blue), oxygen (red), and hydrogen (white).

2.4 | Computations

A two-dimensional relaxed PES scan was performed for azide **1** using the DFT-B3LYP [29–31] functional in conjunction with the 6-311+G(2d,p) basis set [32]. The procedure involved stepwise variation of the two dihedral angles defining the orientation of the azidomethyl group, although all other internal coordinates were optimized (Figure S1). The minimum energy structures identified for **1** and for the photoproducts investigated in this work were fully optimized and subsequently subjected to harmonic vibrational frequency calculations at the same level of theory. The resulting vibrational wavenumbers were scaled by factors of 0.979 below 3000 cm^{-1} and 0.960 above 3000 cm^{-1} and, together with the corresponding IR intensities, were used for spectral simulations [33]. Each band was convoluted with a Lorentzian function with a full width at half maximum (FWHM) of 2 cm^{-1}, centered at the scaled wavenumbers, using the ChemCraft software (Version 1.6) [34]. The integral band intensities correspond to the calculated absolute IR intensities and are reported in arbitrary units as relative intensities. Vibrational mode assignments were performed using vibAnalysis software [35] and by visual inspection of normal-mode animations. To obtain more accurate energies, the relevant species and transition states were subjected to geometry optimizations and harmonic vibrational frequency calculations at the ωB97XD/6-311+G(2d,p) level [36], and single-point energies were subsequently computed at the DLPNO-CCSD(T)/def2-TZVPP level [37–40]. T_1 diagnostics from DLPNO-CCSD(T) calculations

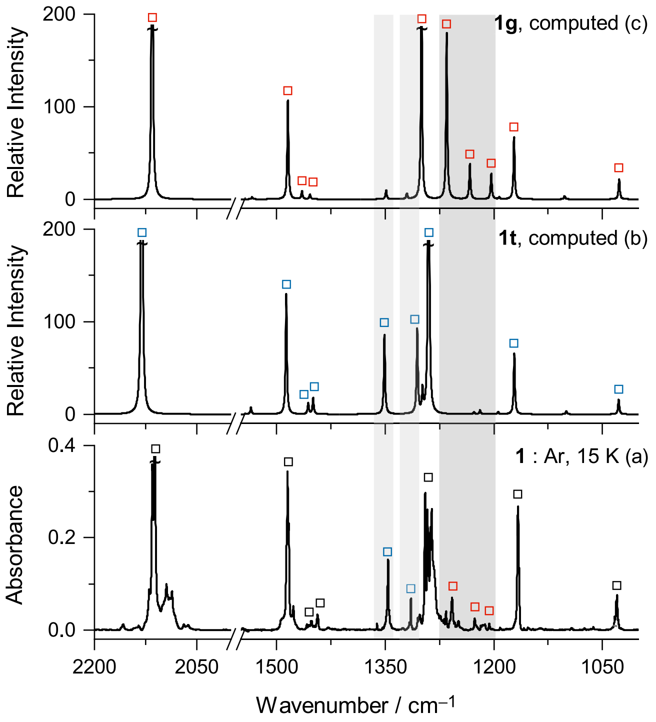

FIGURE 1 | (a) Experimental IR spectrum of 4-azidomethyl-pyridine-*N*-oxide **1** isolated in an Ar matrix at 15 K. (b,c) B3LYP/6-311+G(2d,p) computed IR spectra of *trans* and *gauche* conformers of azide **1** (**1t** and **1g**). The light gray and dark gray backgrounds indicate bands assigned to conformers **1t** (blue squares) and **1g** (red squares), respectively.

(0.016 for $^{3}\mathbf{2}$ and 0.023 for $^{3}\mathbf{3}$ and the corresponding transition state) indicate only limited multireference character, consistent with a reliable coupled-cluster description of these open-shell systems. All DFT computations were carried out with Gaussian 16 (Revision B.01) [41], whereas the coupled-cluster single-point calculations were performed using the ORCA (Version 6.1.0) [42–45]. Hirshfeld atomic spin populations of triplet nitrene $^{3}\mathbf{2}$ and triplet imine $^{3}\mathbf{3E}$ were calculated from B3LYP/6-311+G(2d,p) spin densities using the Multiwfn program [46]. Spin contamination in the B3LYP descriptions of the open-shell triplet species was found to be negligible based on $\langle S^2 \rangle$ values close to the ideal value of 2.000.

3 | Results and Discussion

The conformational space of 4-azidomethyl-pyridine-*N*-oxide **1** was explored at the B3LYP/6-311+G(2d,p) level as a function of rotation around the exocyclic C–C and C–N bonds (Figure S1). Two distinct minima were identified, conformers **1g** (fourfold degenerate) and **1t** (doubly degenerate) (Table 1). In **1g**, the C–N bond is tilted out of the ring plane, and the azide group adopts *gauche* (**g**) orientation relative to the C–C bond. In **1t**, the C–N bond lies approximately in the ring plane, with the azide group

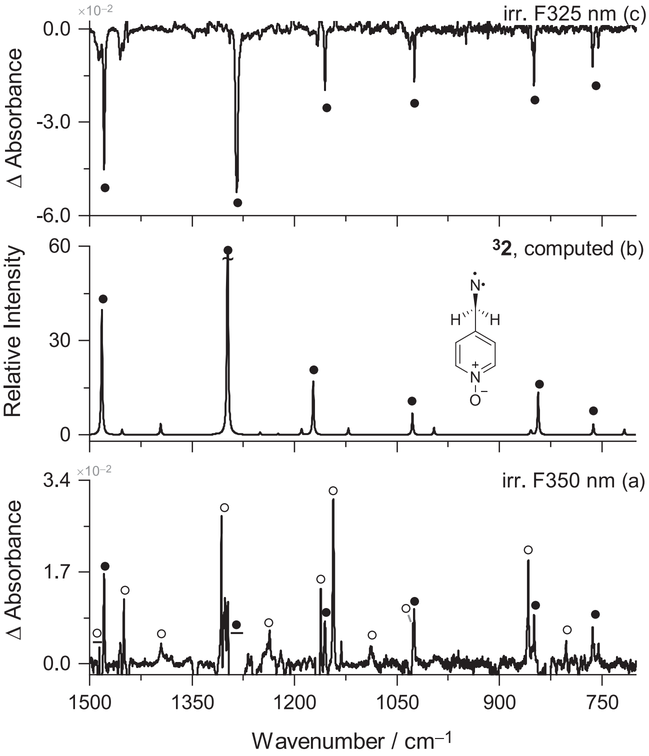

FIGURE 2 | (a) Experimental difference IR spectrum showing changes after irradiation at λ ≥ 350 nm (250 W, 2 min) of 4-azidomethyl-pyridine-*N*-oxide **1** in an Ar matrix at 15 K. Negative bands due to consumption of **1** are truncated. (b) B3LYP/6-311+G(2d,p) computed IR spectrum of triplet 4-nitrenemethyl-pyridine-*N*-oxide $^{3}\mathbf{2}$. (c) Experimental difference IR spectrum showing changes after irradiation at λ ≥ 325 (250 W, 12 min), subsequent to the consumption of **1** at λ ≥ 350 nm (250 W, 1 h). Positive bands due to unidentified products are truncated. Closed circles indicate bands of the photoproduct **A** assigned to $^{3}\mathbf{2}$, and open circles indicate bands of the photoproduct **B**.

TABLE 2 | Experimental IR spectral data (Ar matrix 15 K), B3LYP/6-311+G(2d,p) computed wavenumbers ($\tilde{\nu}$/cm^{-1}) and IR intensities (I/km mol^{-1}), and approximate vibrational assignment of triplet 4-nitrenemethyl-pyridine-*N*-oxide $^{3}\mathbf{2}$.

Experimental[a]	**Calculated**[b]		**Approximate assignment**[c]
Ar, 15 K	$\tilde{\nu}$	**I**	
1624 (w)*	1626	36.6	νCC ring
1479 (s)	1482	125.1	δCH ring; νNO – νCC exo
n.o.	1396	11.3	δCH_2
1286/1283 (s)	1298	252.7	νNO
1156 (m)	1173	53.6	νCC ring; δCH ring
1025 (m)	1027	21.4	νCN ring; δ ring
852/849 (m)	843	42.4	γCH ring; γ ring
763/755 (w)	762	10.6	νCC exo; δ ring

[a] Abbreviation “n.o.” refers to a non-observed band. Asterisk symbol refers to a band partially overlapped with monomeric water. Experimental intensities are expressed in qualitative terms: s, strong; m, medium; w, weak.
[b] Only vibrational modes in the 1800–550 cm^{-1} region having calculated intensities ≥ 10 km mol^{-1} were considered. Harmonic wavenumbers were scaled by 0.979.
[c] Approximate assignment was based on the results provided by the “vibAnalysis” software and supported by ChemCraft animation of the corresponding vibrations. Abbreviations: ν = stretching, δ = in-plane bending, γ = out-of-plane bending; exo = exocyclic fragment. The symbol “–” denotes vibrational combinations occurring in the opposite phase (out-of-phase).

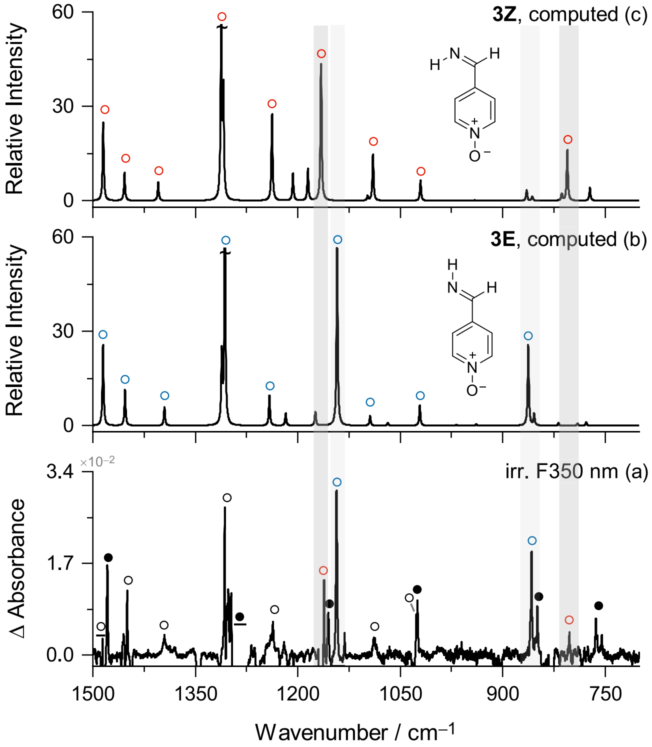

FIGURE 3 | (a) Experimental difference IR spectrum showing changes after irradiation at λ ≥ 350 nm (250 W, 2 min) of 4-azidomethyl-pyridine-*N*-oxide **1** in an Ar matrix at 15 K. Negative bands due to consumption of **1** are truncated. (b,c) B3LYP/6-311+G(2d,p) computed IR spectra of *E* and *Z* isomers of 4-iminomethyl-pyridine-*N*-oxide (**3E** and **3Z**). The light gray and dark gray backgrounds indicate bands assigned specifically to isomer **3E** (blue open circles) and **3Z** (red open circles), respectively.

assuming *trans* (**t**) configuration with respect to the C–C bond. The two conformers are nearly isoenergetic, which is confirmed at the higher DPLNO-CCSD(T)/def2-TZVPP//ωB97XD/6-311+G(2d,p) level. Boltzmann populations calculated from the Gibbs free energies of **1** computed in the gas phase at room temperature indicate that conformers **1g** and **1t** are present in similar proportions (Table 1).

The synthesized 4-azidomethyl-pyridine-*N*-oxide **1** precursor of ^{3}**2** was gently evaporated slightly above room temperature and its vapors were co-deposited with a large excess of Ar onto the cryostat optical window cooled to 15 K. The resulting IR spectrum of monomers of **1** isolated in an Ar matrix reveals the presence of both **1g** and **1t** conformers (Figure 1). In particular, the IR bands at 1346 and 1315 cm^{-1} are in close agreement with the B3LYP computed vibrational modes of **1t** at 1349 and 1306 cm^{-1}, whereas the IR bands at 1258, 1227, and 1206 cm^{-1} are exclusively compatible with the computed vibrational modes of **1g** at 1265, 1233 and 1204 cm^{-1}. A comprehensive assignment of the IR spectrum of **1** is given in Table S1.

The spectroscopic data clearly indicate that in the deposited matrix, the population of **1t** is significantly larger than that of **1g**. These results can be interpreted as follows: Although the computed zero-point-corrected energies suggest that **1g** is marginally more stable than **1t** in the gas phase, under matrix-isolation conditions, the nearly planar **1t** becomes the most energetically favored form due to its better accommodation within the packed

TABLE 3 | Experimental IR spectral data (Ar matrix 15 K), B3LYP/6-311+G(2d,p) computed wavenumbers ($\tilde{\nu}$/cm^{-1}) and IR intensities (I/km mol^{-1}), and approximate vibrational assignment of *E* and *Z* isomers of 4-iminomethyl-pyridine-*N*-oxide, **3E** and **3Z**.

Experimental[a]	**Calculated**[b]			
Ar, 15 K	$\tilde{\nu}$	**I**	**Isomer**	**Approximate assignment**[c]
1639 (w)	1646/1644	65.9/38.5	**3E/3Z**	νC=N
1614 (m)	1623/1620	177.7/183.3	**3E/3Z**	νCC ring; νC=N
1541 (w)	1529/1528	19.0/12.9	**3E/3Z**	[νCC; νCN] ring
1486 (ov)	1485/1485	80.9/78.0	**3E/3Z**	δCH ring; νNO − νCC exo
1450 (m)	1454/1453	27.8/35.7	**3Z/3E**	[νCC; δCH] ring
1395 (br)	1404/1395	18.6/18.5	**3Z/3E**	[δNH; δCH] exo
1307 (s)	1312/1311	189.3/69.4	**3Z/3E**	νNO/δCH ring
1303/1302/1297 (m)	1309/1307	104.0/210.9	**3Z/3E**	δCH ring/νNO
1236 (m)	1241/1238	30.2/86.7	**3E/3Z**	νCN ring; [δNH; δCH] exo; νCC exo
1220 (w)	1218/1207	12.5/27.3	**3E/3Z**	[νCC; νCN] ring
n.o.	1185	31.4	**3Z**	δNH; νCC exo
n.o.	1174	13.9	**3E**	δNH; δCH ring
1161 (m)	1166	136.3	**3Z**	[νCC; δCH] ring
1143 (s)	1142	178.6	**3E**	δNH; νCC exo; δCH ring
1088 (m)	1094/1090	10.0/46.0	**3E/3Z**	δCH ring/[γNH + γCH] exo
1026 (m)	1021/1020	20.3/20.2	**3E/3Z**	νCN ring; δ ring
n.o.	865	10.7	**3Z**	γ ring; γC$_{exo}$; γCH ring; γCH exo; γNH
858 (s)	862	80.5	**3E**	γ ring; γCH ring; γNH
	854	11.3	**3E**	γ Ring breathing
802 (w)	805	51.0	**3Z**	γ ring; γC$_{exo}$; γCH ring; γCH exo; γNH
n.o.	772	13.2	**3Z**	νCC exo; δ ring
n.o.	691	19.9	**3Z**	γ ring; γC$_{exo}$; γCH ring; γCH exo; γNH
593 (m)	596/586	63.1/21.4	**3E/3Z**	δ CC=N; δ ring

[a] Abbreviation "n.o." refers to a non-observed band. Experimental intensities are expressed in qualitative terms: s, strong; m, medium; br = broad; w, weak; ov = overlapped.

[b] Only vibrational modes in the 1800–550 cm^{-1} region having calculated intensities ≥ 10 km mol^{-1} were considered. Harmonic wavenumbers were scaled by 0.979.

[c] Approximate assignment was based on the results provided by the "vibAnalysis" software and supported by ChemCraft animation of the corresponding vibrations. Abbreviations: ν = stretching, δ = in-plane bending, γ = out-of-plane bending; exo = exocyclic fragment. The symbols "+" and "−" denote vibrational combinations occurring in the same phase (in-phase) and in opposite phases (out-of-phase), respectively.

matrix lattice [47–49]. Given the very low energy barrier separating these conformers (~3–5 kJ mol^{-1}: see Figure S2), **1g** partially converts to the lower-energy **1t** during the matrix deposition. This phenomenon, often referred to as conformational cooling, leads to a matrix population of conformational isomers that differs from the original gas-phase equilibrium, which would otherwise be “frozen” under matrix-isolation conditions [50–52].

Irradiation of matrix-isolated azide **1**, using a 350-nm long-pass cutoff filter, results in two primary photoproducts, **A** and **B**, which are the only species detected within the first 2 min (~17% consumption of **1**) (Figure 2a). Upon prolonged irradiation under these conditions, one of the primary products (**B**) decreases its amount in the matrix concomitantly with the continued consumption of **1**, whereas the other (**A**) keeps accumulating (Figures S3 and S4). The secondary photoproducts arising from the consumption of **B** remain unidentified. Subsequent irradiation at shorter wavelengths, using a 325-nm long-pass cutoff filter, consumes the accumulated primary product **A**, thereby enabling a relatively cleaner IR spectral signature to be recorded. The good agreement between the experimental and B3LYP-computed spectra allows us to identify **A** as triplet 4-nitrenemethyl-pyridine-*N*-oxide ^{3}**2** (Figure 2c,b). For instance, the most intense IR bands of ^{3}**2** are observed at 1479 and ~1285 cm^{-1} and are well reproduced by the most intense computed IR absorption at 1482 and 1298 cm^{-1}, respectively. Except for the computed vibrational mode at 1396 cm^{-1} ($I = 11.3$ km mol^{-1}), all other modes of ^{3}**2** with appreciable intensity (≥ 10 km mol^{-1}) were successfully identified in the experimental spectrum, as detailed in Table 2.

Having unambiguously assigned primary product **A** as the triplet nitrene ^{3}**2**, the remaining bands in the IR spectrum recorded after the first 2 min of irradiation of **1** correspond to the spectral signature of the primary product **B** (Figures 2a and 3a). On the basis of these experimental data and supported by B3LYP computations, we identify **B** as 4-iminomethyl-pyridine-*N*-oxide **3**, which exists in two isomeric forms, *E* (**3E**) and *Z* (**3Z**) (Figure 3). For instance, the experimental IR bands observed at 1143 and 858 cm^{-1} show excellent correspondence with the computed IR absorption of **3E** at 1142 and 862/854 cm^{-1}, respectively. In contrast, the experimental IR bands observed at 1161 and 802 cm^{-1} agree well with the computed IR modes of **3Z** at 1166 and 805 cm^{-1}, respectively. For most other regions, the experimental IR spectrum agrees well with the B3LYP-computed spectra of both **3E** and **3Z**, which differ only slightly. A detailed assignment of the IR spectra identifying the two imine isomers **3E** and **3Z** is given in Table 3.

In an additional experiment, after photogeneration of triplet nitrene ^{3}**2** from **1** in an Ar matrix, the sample was kept in the dark for 24 h. IR monitoring revealed no detectable changes, demonstrating that ^{3}**2** is stable under cryogenic matrix conditions over this period. This observation strongly suggests that quantum tunneling 1,2-H shift from ^{3}**2** to imine **3** is not operative on the experimental timescale.

To rationalize these results, we explored the PES connecting triplet nitrene ^{3}**2** with the corresponding triplet imine ^{3}**3** (Figure 4). DPLNO-CCSD(T)//ωB97XD calculations reveal that ^{3}**3** is thermodynamically more stable than ^{3}**2** by more than 10 kcal mol^{-1}. Consequently, the persistence of triplet nitrene ^{3}**2** in the matrix and the absence of a tunneling-driven 1,2-H shift to ^{3}**3** cannot be rationalized on thermodynamic grounds, given the exothermic nature of the rearrangement.

Spin density analysis provides insights into the origin of the relative energy of ^{3}**2** and ^{3}**3** species. As expected for an alkyl nitrene, the spin density in ^{3}**2** is highly localized at the nitrene nitrogen atom, with only minimal delocalization onto the molecular

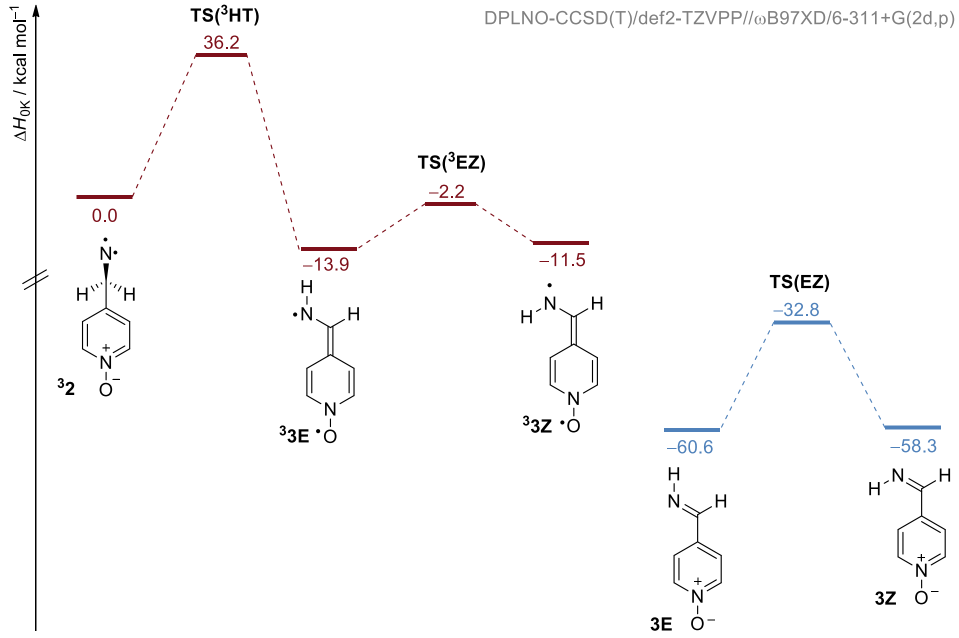

FIGURE 4 | Reaction energy profile (ΔH_{0K} in kcal mol^{-1}) computed at the DPLNO-CCSD(T)/def2-TZVPP//ωB97XD/6-311+G(2d,p) + ZPVE level of theory. Values are relative to the energy of triplet nitrene ^{3}**2**.

framework (Figure 5 and Table 4). In contrast, the triplet imine ^{3}**3** exhibits pronounced spin delocalization over the exocyclic nitrogen, the *ipso* carbon, and the *N*-oxide fragment. This extensive delocalization, strongly enhanced by the *N*-oxide moiety, provides a compelling explanation for the surprising relative stabilization of triplet imine ^{3}**3** (see comparison with the energetics of the benzyl and ethyl derivatives in Figure S5). Consistent with this picture, the computed energy barrier for E/Z isomerization of ^{3}**3** is only ~10 kcal mol^{-1}, indicating that the exocyclic C–N bond possesses significant single-bond character rather than that of a typical imine double bond. Altogether, these data indicate that triplet imine ^{3}**3** is better described as a delocalized diradicaloid species.

Although the rearrangement from ^{3}**2** to ^{3}**3** is thermodynamically allowed, computations predict that this 1,2-H shift has a high-energy barrier of ~36 kcal mol^{-1} (Figure 4). Whereas a few extraordinary examples of H-tunneling reactions through significant energy barriers (~20–30 kcal mol^{-1} range) [18, 53–56] have been reported in noble-gas cryogenic matrices, no tunneling reactions have been observed for barriers on the order of ~36 kcal mol^{-1}. Such a high barrier is therefore expected to effectively suppress 1,2-H shift tunneling from ^{3}**2** to ^{3}**3** under cryogenic conditions[3]. At higher temperatures, however, thermally assisted tunneling may become feasible [53, 57], an intriguing possibility that merits further investigation.

Finally, we can exclude the formation of imine **3** as a secondary product arising from the photochemistry of nitrene ^{3}**2**. Monitoring the photolysis of **1** as a function of time showed that **3** reaches its maximum amount within the first minutes, whereas ^{3}**2** continues to accumulate in the matrix (Figure S4). If imine **3** were formed via nitrene ^{3}**2**, its maximum amount in the matrix would be expected to follow that of ^{3}**2**. Therefore, **3** is most likely formed in competition with ISC to ^{3}**2** from a singlet nitrene ^{1}**2** intermediate generated directly upon photolysis of azide **1** (Scheme 2). Assuming a singlet–triplet energy gap for nitrene **2** comparable to that of methylnitrene (~30 kcal mol^{-1}) [8], the corresponding 1,2-H shift from ^{1}**2** to imine **3** would be highly exothermic, exceeding 80 kcal mol^{-1}, as reported for methylnitrene [9]. The reason why ISC can effectively compete with the ultrafast 1,2-H shift on the singlet surface, enabling the trapping of triplet nitrene ^{3}**2**, as observed for the simple trifluoromethylnitrene [11] but not for methylnitrene [3, 4] remains unclear[4] [58, 59]. Addressing this question will likely require computing the corresponding reaction barriers on the singlet surface using multireference electronic structure methods.

TABLE 4 | Hirshfeld atomic spin population analysis of ^{3}**2** and ^{3}**3E** based on B3LYP/6-311+G(2d,p) calculations.

	Nitrene ^{3}2		**Imine** ^{3}3E	
Atomic space[a]	**Value**	**(%)**	**Value**	**(%)**
N1	1.67	83.7	0.36	18.0
C2	0.11	5.5	0.03	1.5
C3	0.05	2.7	0.32	15.9
C4	0.01	0.4	0.05	2.6
C5	0.00	0.0	0.14	7.2
N6	0.00	0.2	0.31	15.3
O7	0.02	0.8	0.58	28.8
C8	0.00	0.0	0.08	4.2
C9	0.01	0.4	0.08	4.2

[a] Atom numbering starts from the exocyclic nitrogen atom and follows the molecular connectivity in a clockwise direction.

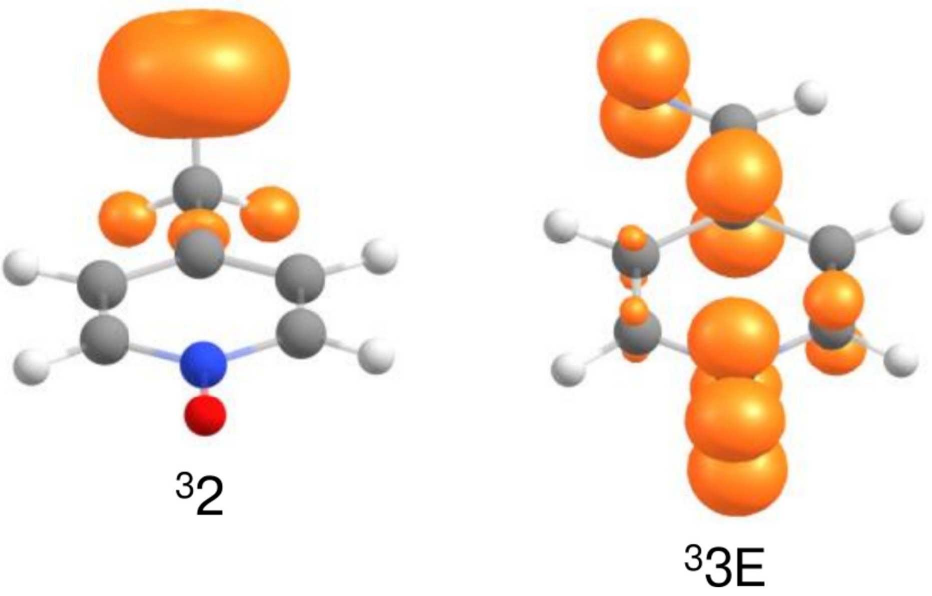

FIGURE 5 | Spin density plots of ^{3}**2** and ^{3}**3E** calculated at the B3LYP/6-311+G(2d,p) level of theory. Isosurfaces are shown at +0.01/−0.01 e bohr^{-3} (orange/cyan). Color scheme: Carbon (gray), nitrogen (blue), oxygen (red), and hydrogen (white).

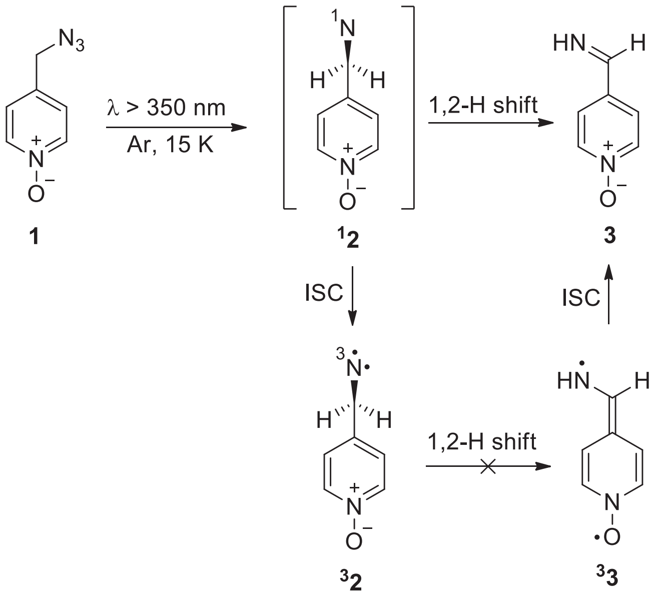

SCHEME 2 | Summary of photolysis of 4-azidomethyl-pyridine-*N*-oxide **1** in an Ar matrix at 15 K. Proposed mechanistic pathways leading to the observed products, triplet nitrene ^{3}**2** and imine **3** via common singlet nitrene ^{1}**2** intermediate, in parallel with the mechanistic interpretation proposed by Platz et al. [11].

4 | Conclusions

This study provided unprecedented experimental access to the simplest triplet alkyl nitrene bearing a pyridine-*N*-oxide moiety, 4-nitrenemethyl-pyridine-*N*-oxide ^{3}**2**, which was generated from photolysis of the 4-azidomethyl-pyridine-*N*-oxide **1** ($\lambda > 350$ nm) isolated in an Ar matrix at 15 K. Alongside, 4-iminomethyl-pyridine-*N*-oxide **3** was also spectroscopically identified as a mixture of E and Z isomers. Monitoring the kinetics of the irradiation process shows that imine **3** does not arise from secondary photochemistry of triplet nitrene ^{3}**2** but is likely formed via an initially unobserved transient singlet nitrene ^{1}**2** in competition with the intersystem crossing to the triplet state.

Triplet nitrene ^{3}**2** remained stable under cryogenic dark conditions, demonstrating that a putative quantum tunneling 1,2-hydrogen shift to the corresponding imine **3E** is not operative on the experimental timescale. Computational analysis reveals that the 1,2-H shift from ^{3}**2** to ^{3}**3E** is thermodynamically favored. The spin density in ^{3}**2** is highly localized on the nitrene nitrogen atom, whereas in ^{3}**3** is strongly delocalized, accounting for the unexpected relative stabilization of the latter. Nevertheless, this reaction involves a substantial energy barrier of ~36 kcal mol^{-1}, effectively precluding H-tunneling under cryogenic temperatures.

Overall, these results expand the fundamental understanding of alkyl nitrene chemistry and establish a well-defined model system for probing fundamental aspects of nitrene reactivity and tunneling phenomena. Furthermore, given that the pyridine-*N*-oxide moiety serves as an anchoring group capable of forming complexes with calix[4]pyrrole derivatives, these findings also open new perspectives for investigating alkyl nitrenes under supramolecular confinement and within host–guest architectures.

Author Contributions

Cláudio M. Nunes: conceptualization, investigation, funding acquisition, writing – original draft, data curation, formal analysis. **A. J. Lopes Jesus:** formal analysis, writing – review and editing, data curation. **Tatiana Caneca:** investigation. **Gemma Aragay:** writing – review and editing, formal analysis, investigation. **Pablo Ballester:** writing – review and editing, formal analysis, funding acquisition. **Rui Fausto:** writing – review and editing, formal analysis, funding acquisition.

Acknowledgments

This work was supported by Project 2023.11222.PEX (https://doi.org/10.54499/2023.11222.PEX) funded by the Fundação para a Ciência e a Tecnologia (FCT), Portuguese Agency for Scientific Research. The authors acknowledge funding from the Coimbra Chemistry Centre—Institute of Molecular Sciences (CQC-IMS) which is supported by the Fundação para a Ciência e a Tecnologia (FCT), Portuguese Agency for Scientific Research. CQC is funded by FCT through projects UID/PRR/00313/2025 (https://doi.org/10.54499/UID/PRR/00313/2025), UID/PRR2/00313/2025 (https://doi.org/10.54499/UID/PRR2/00313/2025), and UID/00313/2025 (https://doi.org/10.54499/UID/00313/2025) and IMS through special complementary funds provided by FCT (project LA/P/0056/2020). The authors also acknowledge FCT Advanced Computing Project 2023.10449.CPCA.A2 and the Laboratory for Advanced Computing at University of Coimbra (UC-LCA) for providing computing resources that have contributed to the research results reported within this paper. R.F. thanks the Horizon-Widera-2023-Talents-01 ERA-Chair 1011848998 Spectroscopy@IKU "Manipulating and Characterizing Molecular Architectures: From Isolated Molecules to Molecular Crystals" funded by the European Union. P.B. and G.A. thank funding from MICIU/AEI/10.13039501100011033 (Severo Ochoa Excellence Accreditation CEX2024-001469-S and project PID2023-149233NB-I00, cofunded by FEDER/UE), the CERCA Program/Generalitat de Catalunya, AGAUR (2021 SGR 00851), and the ICIQ Foundation. Open access publication funding provided by FCT (b-on).

Funding

This work was supported by Fundação para a Ciência e a Tecnologia (FCT), (2023.11222.PEX, UID/PRR/00313/2025, UID/00313/2025, LA/P/0056/2020, 2023.10449.CPCA.A2), European Union Horizon-Widera-2023-Talents-01 ERA-Chair 1011848998, Severo Ochoa Excellence Accreditation (CEX2024-001469-S, PID2023-149233NB-I00), CERCA Program/Generalitat de Catalunya (2021 SGR 00851), and ICIQ Foundation.

Conflicts of Interest

The authors declare no conflicts of interest.

Data Availability Statement

The data that support the findings of this study are available in the Supporting Information of this article.

Endnotes

[1] Some evidence of the triplet methylnitrene, generated, for instance, via metastable energy-transfer fragmentation of methyl azide and methyl isocyanate in matrix-isolation experiments, has been reported based on EPR and UV-Vis spectroscopy; see Ferrante [5, 6].

[2] The generation of hydrogen-bonded complexes of triplet methylnitrene in a cryogenic matrix has been reported recently. see Du et al. [7].

[3] Quantum tunneling probability decreases exponentially with increasing barrier width and with the square root of both the barrier

height and the mass of the tunneling particle. Consequently, an analysis based solely on energetic considerations cannot provide an accurate rationalization of tunneling reactivity. In the present case, the 1,2-H shift from triplet nitrene **3**^{2} to imine **3**^{3} is preceded by a significant reorganization of the heavy-atom framework, most notably a torsional motion of the nitrene fragment toward planarity, which occurs prior to hydrogen migration. Such heavy-atom rearrangements broaden the tunneling barrier and increase the effective mass along the reaction coordinate, thereby substantially reducing the tunneling probability at cryogenic temperatures. A quantitative prediction of tunneling probabilities would therefore require explicit multidimensional tunneling treatments, which are beyond the scope of this work.

[4] The pyrolysis of benzyl azide coupled with matrix isolation did not detect the corresponding triplet nitrene but only the imine derivatives. See Pinto et al. [58, 59].

References

1. M. S. Platz, "Nitrenes," in *Reactive Intermediate Chemistry*, eds. R. A. Moss, M. S. Platz, and M. Jones, Jr. (John Wiley & Sons Inc, 2004).

2. S. Vyas, A. H. Winter, and C. M. Hadad, "Theory and Computation in the Study of Nitrenes and Their Excited-State Photoprecursors," in *Nitrenes and Nitrenium Ions*, eds. D. E. Falvey and A. D. Gudmundsdottir (John Wiley & Sons Inc, 2013).

3. D. E. Milligan, "Infrared Spectroscopic Study of the Photolysis of Methyl Azide and Methyl-D-3 Azide in Solid Argon and Carbon Dioxide," *Journal of Chemical Physics* 35 (1961): 1491–1497.

4. M. E. Jacox and D. E. Milligan, "The Infrared Spectrum of Methylenimine," *Journal of Molecular Spectroscopy* 56 (1975): 333–356.

5. R. F. Ferrante, "Spectroscopy of Matrix-Isolated Methylnitrene," *Journal of Chemical Physics* 86 (1987): 25–32.

6. R. F. Ferrante, "Vibrational Frequencies in the $\tilde{A}\,^3E$ State of Methylnitrene," *Journal of Chemical Physics* 94 (1991): 4678–4679.

7. Y. Du, X. Li, J. Jiang, et al., "Hydrogen-Bonded Complexes of Methylnitrene," *Journal of Physical Chemistry Letters* 16 (2025): 7127–7133.

8. M. J. Travers, D. C. Cowles, E. P. Clifford, G. B. Ellison, and P. C. Engelking, "Photoelectron Spectroscopy of the CH_3N^- Ion," *Journal of Chemical Physics* 111 (1999): 5349–5360.

9. C. R. Kemnitz, G. B. Ellison, W. L. Karney, and W. T. Borden, "CASSCF and CASPT2 Ab Initio Electronic Structure Calculations Find Singlet Methylnitrene Is an Energy Minimum," *Journal of the American Chemical Society* 122 (2000): 1098–1101.

10. C. Larson, Y. Ji, P. Samartzis, et al., "Collision-Free Photochemistry of Methylazide: Observation of Unimolecular Decomposition of Singlet Methylnitrene," *Journal of Chemical Physics* 125 (2006): 133302.

11. N. P. Gritsan, I. Likhotvorik, Z. Zhu, and M. S. Platz, "Observation of Perfluoromethylnitrene in Cryogenic Matrixes," *Journal of Physical Chemistry A* 105 (2001): 3039–3041.

12. I. R. Dunkin and P. C. P. Thomson, "Photolysis of t-Butyl Azide in N_2 at 12 K, and Matrix IR Spectra of Three Isomeric C_4H_9N Imines," *Tetrahedron Letters* 21 (1980): 3813–3816.

13. J. G. Radziszewski, J. W. Downing, M. Jawdosiuk, P. Kovacic, and J. Michl, "4-Azahomoadamant-3-ene: Spectroscopic Characterization and Photoresolution of a Highly Reactive Strained Bridgehead Imine," *Journal of the American Chemical Society* 107 (1985): 594–603.

14. J. G. Radziszewski, J. W. Downing, C. Wentrup, et al., "Geometrical Isomers of a Bridgehead Imine: (E)- and (Z)-2-Azabicyclo[3.2.1]oct-1-ene, and 2-Azabicyclo[2.2.2]oct-1-ene," *Journal of the American Chemical Society* 107 (1985): 2799–2801.

15. S. Muthukrishnan, R. A. A. U. Ranaweera, and A. D. Gudmundsdottir, "Triplet Alkyl Nitrenes," in *Nitrenes and Nitrenium Ions*, eds. D. E. Falvey and A. D. Gudmundsdottir (John Wiley & Sons Inc, 2013).

16. P. N. D. Singh, S. M. Mandel, J. Sankaranarayanan, et al., "Selective Formation of Triplet Alkyl Nitrenes From Photolysis of β-Azido-Propiophenone and Their Reactivity," *Journal of the American Chemical Society* 129 (2007): 16263–16272.

17. P. N. D. Singh, S. M. Mandel, R. M. Robinson, et al., "Photolysis of α-Azidoacetophenones: Direct Detection of Triplet Alkyl Nitrenes in Solution," *Journal of Organic Chemistry* 68 (2003): 7951–7960.

18. C. M. Nunes, S. N. Knezz, I. Reva, R. Fausto, and R. J. McMahon, "Evidence of a Nitrene Tunneling Reaction: Spontaneous Rearrangement of 2-Formyl Phenylnitrene to an Imino Ketene in Low-Temperature Matrixes," *Journal of the American Chemical Society* 138 (2016): 15287–15290.

19. C. M. Nunes, L. P. Viegas, S. A. Wood, J. P. L. Roque, R. J. McMahon, and R. Fausto, "Heavy-Atom Tunneling Through Crossing Potential Energy Surfaces: Cyclization of a Triplet 2-Formylarylnitrene to a Singlet 2,1-Benzisoxazole," *Angewandte Chemie International Edition* 59 (2020): 17622–17627.

20. J. P. L. Roque, C. M. Nunes, L. P. Viegas, et al., "Switching on H-Tunneling Through Conformational Control," *Journal of the American Chemical Society* 143 (2021): 8266–8271.

21. R. Fausto, G. O. Ildiz, and C. M. Nunes, "IR-Induced and Tunneling Reactions in Cryogenic Matrices: The (Incomplete) Story of a Successful Endeavor," *Chemical Society Reviews* 51 (2022): 2853–2872.

22. C. M. Nunes, J. P. L. Roque, S. Doddipatla, S. A. Wood, R. J. McMahon, and R. Fausto, "Simultaneous Tunneling Control in Conformer-Specific Reactions," *Journal of the American Chemical Society* 144 (2022): 20866–20874.

23. J. P. L. Roque, C. M. Nunes, P. R. Schreiner, and R. Fausto, "Hydrogen Tunneling Exhibiting Unexpectedly Small Primary Kinetic Isotope Effects," *Chemistry—A European Journal* 30 (2024): e202401323.

24. A. Galan and P. Ballester, "Stabilization of Reactive Species by Supramolecular Encapsulation," *Chemical Society Reviews* 45 (2016): 1720–1737.

25. L. Adriaenssens, J. L. A. Sánchez, X. Barril, C. K. O'Sullivanbe, and P. Ballester, "Binding of Calix[4]Pyrroles to Pyridine-N-Oxides Probed With Surface Plasmon Resonance," *Chemical Science* 5 (2014): 4210–4215.

26. L. Escobar, Q. Sun, and P. Ballester, "Aryl-Extended and Super Aryl-Extended Calix[4]Pyrroles: Design, Synthesis, and Applications," *Accounts of Chemical Research* 56 (2023): 500–513.

27. Y. Li, C. F. M. Mirabella, G. Aragay, and P. Ballester, "Acceleration and Selectivity of 1,3-Dipolar Cycloaddition Reactions Included in a Polar [4 + 2] Octa-imine Bis-calix[4]pyrrole Cage," *JACS Au* 5 (2025): 902–912.

28. M. Piccinno, G. Aragay, F. Y. Mihan, P. Ballester, and A. Dalla Cort, "Unexpected Emission Properties of a 1,8-Naphthalimide Unit Covalently Appended to a Zn–Salophen," *European Journal of Inorganic Chemistry* 2015 (2015): 2664–2670.

29. A. D. Becke, "Density-Functional Thermochemistry. III. The Role of Exact Exchange," *Journal of Chemical Physics* 98 (1993): 5648–5652.

30. C. Lee, W. Yang, and R. G. Parr, "Development of the Colle-Salvetti Correlation-Energy Formula Into a Functional of the Electron Density," *Physical Review B: Condensed Matter* 37 (1988): 785–789.

31. S. H. Vosko, L. Wilk, and M. Nusair, "Accurate Spin-Dependent Electron Liquid Correlation Energies for Local Spin Density Calculations: A Critical Analysis," *Canadian Journal of Physics* 58 (1980): 1200–1211.

32. M. J. Frisch, J. A. Pople, and J. S. Binkley, “Self-Consistent Molecular Orbital Methods 25. Supplementary Functions for Gaussian Basis Sets,” *Journal of Chemical Physics* 80 (1984): 3265–3269.

33. C. M. Nunes, A. K. Eckhardt, I. Reva, R. Fausto, and P. R. Schreiner, “Competitive Nitrogen Versus Carbon Tunneling,” *Journal of the American Chemical Society* 141 (2019): 14340–14348.

34. G. A. C. Zhurko, “Chemcraft, Version 1.8,” (2016), accessed June 2024, http://www.chemcraftprog.com.

35. F. Teixeira and M. N. D. S. Cordeiro, “Improving Vibrational Mode Interpretation Using Bayesian Regression,” *Journal of Chemical Theory and Computation* 15 (2019): 456–470.

36. J.-D. Chai and M. Head-Gordon, “Long-Range Corrected Hybrid Density Functionals With Damped Atom–Atom Dispersion Corrections,” *Physical Chemistry Chemical Physics* 10 (2008): 6615–6620.

37. A. Jiang, Z. L. Glick, D. Poole, J. M. Turney, C. D. Sherrill, and H. F. Schaefer, “Accurate and Efficient Open-Source Implementation of Domain-Based Local Pair Natural Orbital (DLPNO) Coupled-Cluster Theory Using a t1-Transformed Hamiltonian,” *Journal of Chemical Physics* 161 (2024): 082502.

38. Y. Guo, C. Riplinger, U. Becker, et al., “Communication: An Improved Linear Scaling Perturbative Triples Correction for the Domain Based Local Pair-Natural Orbital Based Singles and Doubles Coupled Cluster Method [DLPNO-CCSD(T)],” *Journal of Chemical Physics* 148 (2018): 011101.

39. F. Weigend and R. Ahlrichs, “Balanced Basis Sets of Split Valence, Triple Zeta Valence and Quadruple Zeta Valence Quality for H to Rn: Design and Assessment of Accuracy,” *Physical Chemistry Chemical Physics* 7 (2005): 3297–3305.

40. F. Weigend, “Accurate Coulomb-Fitting Basis Sets for H to Rn,” *Physical Chemistry Chemical Physics* 8 (2006): 1057–1065.

41. M. J. Frisch, G. W. Trucks, H. B. Schlegel, et al., “Gaussian 16, Revision B.01,” Gaussian Inc., (2016).

42. F. Neese, “Software Update: The ORCA Program System—Version 6.0,” *WIREs Computational Molecular Science* 15 (2025): e70019.

43. F. Neese, “The SHARK Integral Generation and Digestion System,” *Journal of Computational Chemistry* 44 (2023): 381–396.

44. M. Garcia-Ratés and F. Neese, “Effect of the Solute Cavity on the Solvation Energy and Its Derivatives Within the Framework of the Gaussian Charge Scheme,” *Journal of Computational Chemistry* 41 (2020): 922–939.

45. F. Neese, “An Improvement of the Resolution of the Identity Approximation for the Formation of the Coulomb Matrix,” *Journal of Computational Chemistry* 24 (2003): 1740–1747.

46. T. Lu and F. Chen, “Multiwfn: A Multifunctional Wavefunction Analyzer,” *Journal of Computational Chemistry* 33 (2012): 580–592.

47. I. D. Reva, S. V. Ilieva, and R. Fausto, “Conformational Isomerism in Methyl Cyanoacetate: A Combined Matrix-Isolation Infrared Spectroscopy and Molecular Orbital Study,” *Physical Chemistry Chemical Physics* 3 (2001): 4235–4241.

48. A. Gómez-Zavaglia and R. Fausto, “Low Temperature FT-IR and Molecular Orbital Study of N,N-Dimethylglycine Methyl Ester: Proof for Different Ground Conformational States in Gas Phase and in Condensed Media,” *Physical Chemistry Chemical Physics* 5 (2003): 52–63.

49. I. D. Reva, S. G. Stepanian, L. Adamowicz, and R. Fausto, “Conformational Behavior of Cyanoacetic Acid: A Combined Matrix Isolation Fourier Transform Infrared Spectroscopy and Theoretical Study,” *Journal of Physical Chemistry A* 107 (2003): 6351–6359.

50. I. D. Reva, A. M. Plokhotnichenko, S. G. Stepanian, et al., “The Rotamerization of Conformers of Glycine Isolated in Inert Gas Matrices. An Infrared Spectroscopic Study,” *Chemical Physics Letters* 232 (1995): 141–148.

51. A. Borba, A. Gómez-Zavaglia, and R. Fausto, “Conformational Cooling and Conformation Selective Aggregation in Dimethyl Sulfite Isolated in Solid Rare Gases,” *Journal of Molecular Structure* 794 (2006): 196–203.

52. I. D. Reva, S. G. Stepanian, L. Adamowicz, and R. Fausto, “Missing Conformers. Comparative Study of Conformational Cooling in Cyanoacetic Acid and Methyl Cyanoacetate Isolated in Low Temperature Inert Gas Matrixes,” *Chemical Physics Letters* 374 (2003): 631–638.

53. J. P. L. Roque, C. M. Nunes, E. Ntungwe, A. Fernández-Ramos, and R. Fausto, “Hydrogen Tunneling in Thiobenzamide: A Case Study on Tunneling Through High-Energy Barriers,” *Journal of Organic Chemistry* 90 (2025): 10476–10486.

54. H. Rostkowska, L. Lapinski, and M. J. Nowak, “Hydrogen-Atom Tunneling Through a Very High Barrier; Spontaneous Thiol → Thione Conversion in Thiourea Isolated in Low-Temperature Ar, Ne, H_2 and D_2 Matrices,” *Physical Chemistry Chemical Physics* 20 (2018): 13994–14002.

55. H. Rostkowska, L. Lapinski, A. Khvorostov, and M. J. Nowak, “Proton-Transfer Processes in Thiourea: UV Induced Thione → Thiol Reaction and Ground State Thiol → Thione Tunneling,” *Journal of Physical Chemistry* 107 (2003): 6373–6380.

56. A. K. Eckhardt, F. R. Erb, and P. R. Schreiner, “Conformer-Specific [1,2]H-Tunnelling in Captodatively-Stabilized Cyanohydroxycarbene $(\mathrm{NC - \ddot{C} - OH})$†,” *Chemical Science* 10 (2019): 802–808.

57. E. M. Greer, K. Kwon, A. Greer, and C. Doubleday, “Thermally Activated Tunneling in Organic Reactions,” *Tetrahedron* 72 (2016): 7357–7373.

58. R. M. Pinto, M. Guerra, G. Copeland, et al., “The Mechanism of Pyrolysis of Benzyl Azide: Spectroscopic Evidence for Benzenemethanimine Formation,” *Journal of Physical Chemistry A* 119 (2015): 4118–4126.

59. C. Wentrup, “Comment on ‘the Mechanism of Pyrolysis of Benzyl Azide: Spectroscopic Evidence for Benzenemethanimine Formation’,” *Journal of Physical Chemistry A* 119 (2015): 8256–8257.

Supporting Information

Additional supporting information can be found online in the Supporting Information section. **Figure S1:** Two-dimensional map of the potential energy of 4-azidomethyl-pyridine-*N*-oxide **1** as a function of the C–C–C–N and C–C–N–N dihedral angles. Each dihedral was incremented by 10°, with all remaining structural parameters fully optimized at the B3LYP/6-311+G(2d,p) level. Energy minima are denoted as **1g** (fourfold degenerate) and **1t** (doubly degenerate). The color scale corresponds to relative energies, referenced to the lowest minimum (**1g**), and isoenergy lines are drawn every $1\,\mathrm{kJ\,mol^{-1}}$. **Figure S2:** Potential energy diagram showing the relative zero-point-corrected energies of the **1g** and **1t** conformers of 4-azidomethyl-pyridine-*N*-oxide **1**, together with the transition state along the minimum energy path connecting the two conformers. The energy of the most stable conformer (**1g**) was taken as the zero of the relative energy scale. The energies shown were computed at the B3LYP/6-311+G(2d,p) (blue) and ωB97XD/6-311+G(2d,p) (red) levels of theory. **Figure S3:** Experimental IR difference spectra showing the spectral changes observed after 2 min of UV irradiation ($\lambda \geq 350\,\mathrm{nm}$), followed by an additional 13 min of irradiation (15 min total) under identical conditions, of 4-azidomethyl-pyridine-*N*-oxide **1** isolated in an Ar matrix at 15 K. Positive and negative bands correspond to photogenerated and consumed species, respectively. The spectral changes indicate that the primary photoproducts **A** (assigned to triplet 4-nitrenemethyl-pyridine-*N*-oxide $^{3}\mathbf{2}$) and **B** (assigned to 4-iminomethyl-pyridine-*N*-oxide **3**) are both formed within the first 2 min of irradiation. Upon prolonged irradiation, **B** is consumed concomitantly with **1**, whereas **A** continues to accumulate in the matrix. Bands marked with an asterisk are assigned unidentified secondary photoproducts. **Figure S4:** Time evolution of the amounts of 4-azidomethyl-pyridine-*N*-oxide **1** and of its photoproducts 4-nitrenemethyl-pyridine-*N*-oxide ^{3}**2** and the **E**- and **Z**-isomers of 4-iminomethyl-pyridine-*N*-oxide during UV exposure ($\lambda \geq 350$ nm) of **1** isolated in an Ar matrix at 15 K for 15 min. The relative concentrations of reactant **1** and photoproducts ^{3}**2**, **3E**, and **3Z** were estimated from the integrated areas of their characteristic infrared bands. Initially, diagnostic bands were selected based on their high intensity and absence of overlap with other spectral features: 1346 cm^{-1} (**1**), 1156 cm^{-1} (^{3}**2**), 1143 cm^{-1} (**3E**), and 1161 cm^{-1} (**3Z**). To account for the different transition dipole moments of these vibrations, the experimental integrated intensities were divided by the calculated intensities of the corresponding vibrations obtained from the B3LYP/6-311+G(2d,p) calculations (see Tables 2, 3, and S1). In the final step, these weighted integrated intensities were scaled by a common normalization factor, setting the initial amount of reactant **1** at $t = 0$ min to 100%. At the early stages of photolysis ($t \leq 2$ min), the sum of all identified species remains close to 100%. At longer irradiation times, this proportion decreases to 77% at $t = 4$ min and to 62% at $t = 15$ min, reflecting the formation of additional, unidentified secondary photoproducts, which account for the remaining 23% and 38%, respectively. **Figure S5:** Reaction energy profile (ΔH_{0K} in kcal mol^{-1}) computed at the ωB97XD/6-311+G(2d,p) + ZPVE level of theory for the 1,2-H shift from triplet alkyl nitrenes to the corresponding imines. Values are relative to the energy of the corresponding triplet alkyl nitrenes. **Table S1:** Experimental IR spectral data for azide 4-azidomethyl-pyridine-*N*-oxide **1** isolated in an Ar matrix at 15 K, compared with the B3LYP/6-311+G(2d,p) vibrational frequencies (ν, cm^{-1}) and infrared intensities (I, km mol^{-1}) calculated for the two conformers of **1** (**1g** and **1t**) and approximate vibrational assignments^{a}.